Image and Vision Computing 27 (2009) 771–781

Contents lists available at ScienceDirect

Image and Vision Computing

journal homepage: www.elsevier.com/locate/imavis

Statistics and category systems for the shape index descriptor of local 2nd order natural image structure

Martin Lillholm *, Lewis D. Griffin

Department of Computer Science, University College London, Malet Place, London WC1E 6BT, United Kingdom

ARTICLE INFO

Article history:
Received 14 May 2007
Received in revised form 4 August 2008
Accepted 4 August 2008

Keywords:
Local image structure
Image features
Natural image statistics

ABSTRACT

The shape index offers a natural and invariant description of pure 2nd order image structure. We discuss its properties and report novel natural image statistics for the shape index and the additional two parameters of curvedness and principal direction that form a complete and decoupled re-parameterisation of 2nd order structure. In a second main theme, we address three separate avenues to a categorisation of the shape index for natural images and suggest five feature categories as a natural 2nd order image structure 'alphabet'.

1. Introduction

The notions of local image structure and image features are as old as the field of computer vision itself. Both topics has always attracted much attention and the literature is vast. Although much progress has been made, complete lists of local structure types or features in say natural images still seem elusive and most approaches based on features are constrained by the availability of feature detectors more or less suited for the tasks at hand. Our aim with this paper is to investigate the feature types governed by 2nd order structure of natural images. We will continue this introduction with a short review of the ideas that have dominated the way features are conceived, describe our overall approach, and give a summary of how we choose to measure quantitative image structure.

1.1. Quantitative and qualitative local image structure

Local image structure in its simplest form can be described through the pixels in a neighbourhood around a point – typically in form of a patch of image pixels. Although pure patch based descriptions have recently had a revival [52,8,58,1], a next step has been to apply a bank of filters to the image patches to further facilitate analysis – often this is realised without explicit patch extraction using convolution across the entire image. Many collections of filters have been proposed over time: Gabor Filters, Wavelets, and derivatives of Gaussians [24,40,57,25]. The output of such filter banks is typically a response vector in an N-dimensional response space. Many vision algorithms use these *quantitative* descriptions of local image structure directly and with great success [4,61,11,7]. Nevertheless, it remains an intriguing question whether local image structure can be described through a limited alphabet of *qualitative* distinct letters or feature types. Filter responses have been used as the basis for a number of feature detectors [41,3,20,38,38,39] – all of these are, however, results of conscious design choices and do not bring us much closer to answering the posed question.

The main aim of this work is to investigate whether such an alphabet naturally arises from geometrical and statistical studies of a simple model of early visual processing (a filter bank) exposed to natural image stimuli. We adopt the general notion that an alphabet can be found through a partitioning [29,26,31,35,54,60,15,17] of response space into categories of qualitatively similar structures. We will, however, refine this and rather discuss the partitioning of a *factored* response space. A description that factors out extrinsic factors such as translation, orientation, and absolute grey value and generally provides a lower dimensional and more invariant starting point than the full response space. As mentioned above, we focus on the 2nd order structure in this work and thus another aim of the paper is to describe and discuss a suitable factored response space and its properties for natural images – see Section 2.

In terms of categorising or partitioning the factored response space, we will investigate three separate approaches. One is based on the idea of categories being defined as Voronoi cells around prototypes [12]. The second approach is inspired by Koenderink [29,26,31] and refined through Geometric Texton Theory [15,17]. Here the category structure is induced through qualitative similarity of canonical representatives across response space. In the third

* Corresponding author. Tel.: +44 0 20 7679 0332; fax: +44 0 20 7387 1397.
E-mail address: m.lillholm@cs.ucl.ac.uk (M. Lillholm).

0262-8856/$ - see front matter © 2008 Elsevier B.V. All rights reserved.
doi:10.1016/j.imavis.2008.08.003

and final approach, we consider stability – a desirable quality of any category system and investigate the most stable category systems under simple image perturbations such as additive Gaussian noise. These ideas are presented in Section 3.

1.2. Quantitative measurements through Gaussian derivatives

The output of V1 simple cells are modelled as the inner product of Receptive Field weighting functions (RFs) and the retinal irradiance [22]. Several models of V1 simple cell ensembles such as Gabor filters have been reported in the literature [6,24].

In this work we, however, prefer the Gaussian Derivatives (DtGs) as an uncommitted model to measure local image structure. Several arguments favour the DtGs: in terms of biological relevance DtGs up to 4th or 5th order provide a well fitting set of models (a simple linear combination brings the DtGs into the 'wave-train' basis very similar to Gabors [59,30]). It was recently demonstrated [14] that DtGs provide as good a fit to reported Gabors as, e.g. filters obtained from ICA [2,53,23] or sparse coding [44] based approaches. Furthermore, the DtGs are well studied and have many attractive properties [25,28,10,32,14]. The real strength of DtGs is that the measured quantities are much easier to interpret than corresponding Gabors. Local measurements of an image with DtGs up to some order n is also referred to as the n-jet. The n-jet can be understood as the coefficients of truncated Taylor-series of the *blurred* image.

The one-dimensional Gaussian kernel of is given by $G(x) = \frac{1}{\sqrt{2\pi\sigma^2}} \exp\frac{-x^2}{2\sigma^2}$, where σ is the standard deviation and controls the scale or *blur* at which the jet is calculated. Due to separability the two-dimensional Gaussian kernel is easily constructed as $G(x,y) = G(x)G(y)$. We will use G_x, G_{xy}, etc. to denote partial derivatives of the two-dimension kernel and L_{xy} to denote the inner product between an image patch L and the suitable derivative of the Gaussian, i.e. $L_{xy} = \int_{\vec{r}\in\mathbb{R}^2} G_{xy}(\vec{r})L(\vec{r})d\vec{r}$. The n-jet is the vector of inner products up to total order of derivation n – the 2-jet is thus given by $(L, L_x, L_y, L_{xx}, L_{xy}, L_{yy})$.

2. Intrinsic 2nd order structure and the shape index

The first focus of the paper is an investigation of 'pure' 2nd order structure in natural images. In the following, we motivate that this is best studied through the *shape index* and present properties and novel statistics of this descriptor.

2.1. Shape index, curvedness, and principal direction

Through the Gaussian derivative framework we have access to the full set of image derivatives and can study local image structure in this context. As discussed above, this study focuses on the pure second order structure – essentially given by the 2nd order derivatives L_{xx}, L_{xy}, L_{yy}. This characterisation compounds several aspects of local image structure in an undesirable fashion. This includes several *extrinsic* factors that are normally considered irrelevant: the second order derivatives are affected by, e.g. overall image intensity and orientation. A simple affine intensity transformation or image rotation will change the second order derivatives although the local *intrinsic* image structure or 'shape' is unchanged by such transformations. The traditional approach to such problems is to seek a more invariant and uncoupled characterisation. Although the traditional surface invariants, the Gaussian (**K**) and mean curvature (**H**), are rotationally invariant and offer some insight into the intrinsic 'local shape' they do not give the full story and offer an entangled description of shape and contrast.

The shape index ϑ has been suggested by Koenderink [33,34] to give a simple measure of local shape. Like the Gaussian and mean curvature, the shape index can be defined through the principal curvatures (given by the eigenvalues κ_1, κ_2 of the local Hessian H):

$$H = \begin{pmatrix} L_{xx} & L_{xy} \\ L_{xy} & L_{yy} \end{pmatrix}$$

$$\vartheta = \arctan\frac{\kappa_1+\kappa_2}{\kappa_1-\kappa_2} = -\arctan\left(\frac{L_{xx}+L_{yy}}{\sqrt{(L_{xx}-L_{yy})^2+4L_{xy}^2}}\right) \in \left[-\frac{\pi}{2}, \frac{\pi}{2}\right].$$

The shape index is undefined for $\kappa_1 = \kappa_2 = 0$ which make sense as this indicates a flat or structureless point.[1] Strictly speaking, the curvatures $\kappa_{1,2}$ are from the non-standard differential geometry of the singly isotropic spaces see, e.g. [32,34].

At the extremes of the shape index interval, we have concave and convex umbilic-like minima and maxima. A shape index of zero indicates a saddle-like local structure. The mid-points of each of the half-intervals represent concave and convex parabolic- or line-like points. These 'landmarks' are indicated across the shape index interval in Fig. 1.

The shape index is invariant with respect to extrinsic factors such as orientation, absolute gray-value, and translation. A full treatise of the shape index's many commendable properties can be found in [34,33].

For local pure 2nd order structure, the shape index constitutes the factored jet-space discussed in Section 1. In Sections 2.2 and 2.3, we will explore the statistics and canonical natural image representatives of the shape index. Although, the shape index is the main focus of this paper, it is, however, worthwhile to briefly discuss the full re-parameterisation of 2nd order structure that usually accompanies the shape index namely *curvedness* and *principal direction* [34,33].

Given, e.g. two convex parabolic points, that are identical under the shape index descriptor, they may be more or less 'curved' and/or oriented differently. This is precisely one of the strengths of the invariant shape index – sometimes it is, however, desirable to examine these two additional local 2nd order properties as well.

The amount of contrast or curvature is normally formalised through the curvedness λ [34,33]:

$$\lambda = \sqrt{\frac{\kappa_1^2+\kappa_2^2}{2}} = \frac{1}{\sqrt{2}}\sqrt{L_{xx}^2+2L_{xy}^2+L_{yy}^2}$$

Curvedness is also known as total variation or Casorati curvature [5]. It is inversely proportional to the local 'size' and unlike the dimensionless shape index, the curvedness has dimension of reciprocal length. The scaling constant can be omitted but makes the curvedness match the absolute value of one over radius in the spherical case [33]. The curvedness offers an intuitive measure of the 2nd order amplitude. Furthermore, the curvedness only vanishes for truly flat[2] ($k_1 = k_2 = 0$) points whereas the mean and Gaussian curvature also vanishes for saddle ($k_1 = -k_2$) and parabolic points ($k_1 \neq 0, k_2 = 0$), respectively. Fig. 2 gives an example of an image and the corresponding curvedness landscape.

Finally, the principal direction ψ is the direction of the main (signed) curvature. ψ can be found as the direction of the eigenvector belonging to the largest eigenvalue of the Hessian matrix H or directly [34] as:

$$\psi = \frac{1}{2}\arctan\frac{L_{xy}}{\frac{L_{xx}-L_{yy}}{2}} \in \left[-\frac{\pi}{2}, \frac{\pi}{2}\right]$$

An example of an image and its corresponding principal direction landscape can be seen in Fig. 2.

[1] Flatness is here used in the 2nd order sense.
[2] As before, flatness is used in the 2nd order sense.

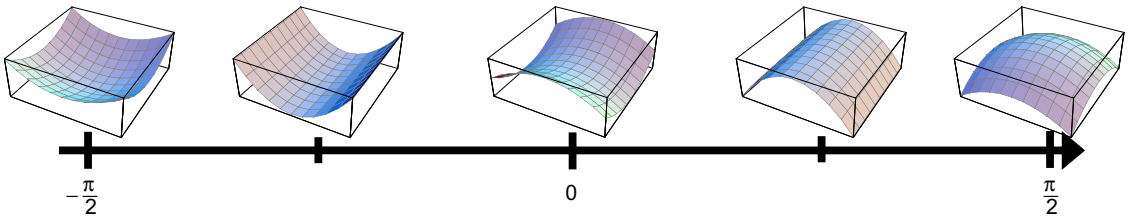

Fig. 1. The shape index range from $-\frac{\pi}{2}$ to $\frac{\pi}{2}$ includes all local (2nd order) surface types. At the extremes, we have umbilical minima and maxima. Shape index zero indicates a saddle-like local structure and the mid-points of the two half-intervals indicate concave and convex parabolic-like structure. The figures above the interval illustrates this but are only examples of surface structures with the corresponding shape index.

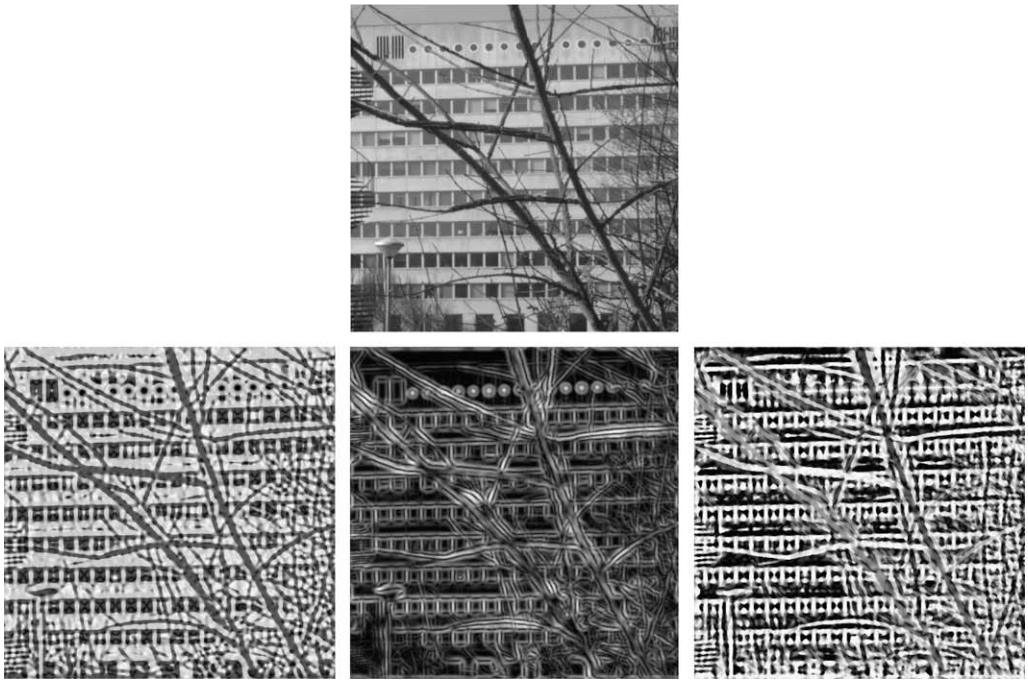

Fig. 2. An example image (top) and corresponding shape index (left), curvedness (middle), and principal direction (right) landscapes.

Summarising, the triple $(\vartheta, \lambda, \psi)$ gives a far more intuitive and decoupled description of the local 2nd order structure than the traditional cartesian triple (L_{xx}, L_{xy}, L_{yy}). Specifically, the shape index is the natural factored response space for 2nd order local image structure. In the following section, we investigate the statistics for each of the three parameters ϑ, λ, ψ over an ensemble of natural images.

2.2. Shape index statistics for natural images and otherwise

In [34], Koenderink investigated the statistics of the shape index, the curvedness, and the principal direction for Gaussian random images and derived the joint distribution of ϑ, λ, and ψ as:

$$P(\lambda, \vartheta, \psi) = \frac{\lambda^2 \sigma^6 \cos\vartheta}{64\pi^3\sqrt{2}} e^{-\frac{\sigma^4}{64\pi}\lambda^2(3+\cos 2\vartheta)},$$

yielding the following marginals:

$$P(\vartheta) = \frac{2\sqrt{2}\cos\vartheta}{(3+\cos 2\vartheta)^{\frac{3}{2}}}, \quad P(\lambda) = \frac{\sigma^4}{8\pi}\lambda \operatorname{erfi}\left(\frac{\sigma^2}{4\sqrt{2\pi}}\lambda\right) e^{-\frac{\sigma^4}{16\pi}\lambda^2},$$
$$P(\psi) = \frac{1}{\pi}.$$

Here erfi is the 'imaginary error function' with $\operatorname{erfi}(z) = -i\operatorname{erf}(iz)$.

To validate the experimental setup for natural images, we have empirically verified the results for Gaussian noise using a database of Gaussian white noise images. Results for Gaussian, Brownian (or pink) noise images can be seen in rows 1 and 2 of Fig. 3. From left to right each row contains the histograms of the shape index, the principal direction, and the curvedness. The Gaussian results are a near perfect match to the analytical distributions given above and as such serve their purpose of validation.

In [34], Koenderink gave the statistics of shape index and curvedness for a single natural image – these more or less matched the Gaussian random image results. It is, however, interesting to see whether this holds for natural images in general. Likewise for the distribution of principal directions which is trivially uniform in the Gaussian case above. The standard procedure for such studies is to report statistics across a (large) ensemble of natural images and not just single fiducial images. Numerous paper has been published on natural image statistics, e.g. [9,49,21,53] using more or less sizeable databases to represent the somewhat vague term natural images. We follow recent trends [53,23,46,19] and use the van Hateren *Natural Stimuli Collection* as a example of a substantial collection of natural images. Specifically, we only use 1220 of the images from the database – see [17] for details. The overall procedure is otherwise identical to the validation of the Gaussian cases described above.

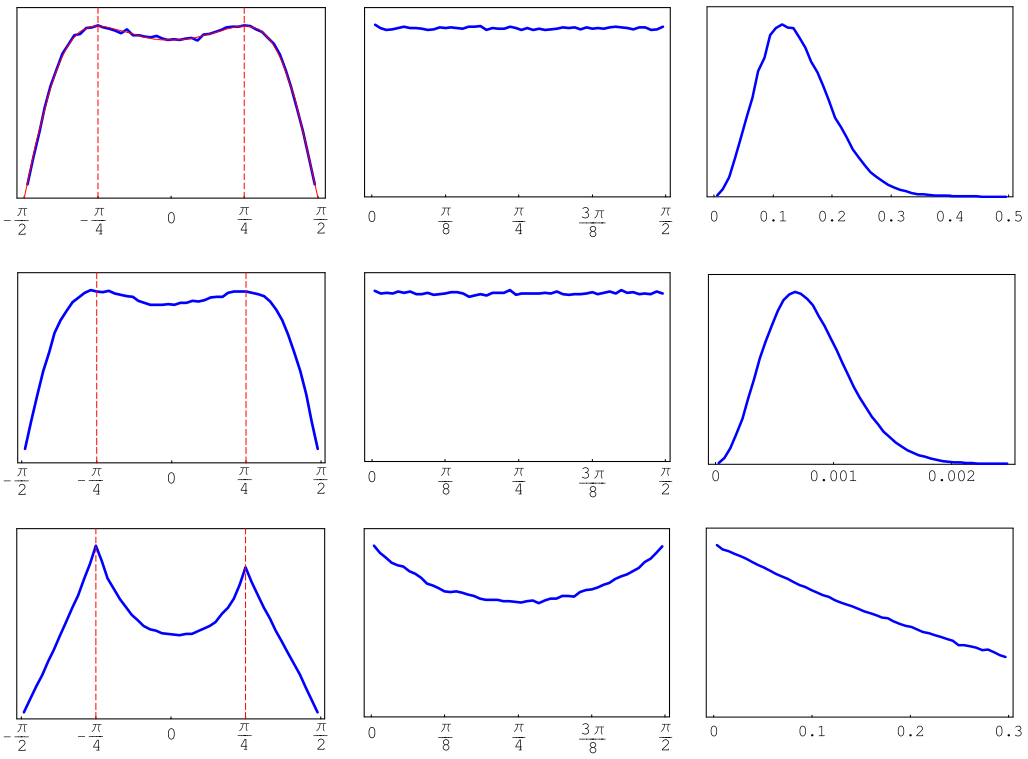

Fig. 3. The histograms of shape index (left), principal direction (middle), and curvedness (right) for Gaussian noise (top), Brownian noise (middle), and natural images (bottom). For clarity the histogram of natural image curvedness (bottom, right) has been logged. The dashed red lines in the left column indicates the parabolic points (convex and concave) at shape indices $-\frac{\pi}{4}$ and $\frac{\pi}{4}$, respectively.

The results for natural images can be seen in Fig. 3, bottom row. Some observations for natural images, beyond those given in [34], are as follows:

- The histogram of shape indices is slightly asymmetric compared to the Gaussian cases and Koenderink's histogram for a single image [34]. The bias is towards dark parabolic-like structures.
- The modes of the natural image shape index histogram are more kurtosed than the corresponding Gaussian and Brownian noise histograms. Like the corresponding modes in the Gaussian cases, they are centred on the parabolic points as indicated by the dashed red lines in Fig. 3.
- The histogram of principal directions (Fig. 3, bottom row, middle) shows a bias towards horizontal and vertical structures. In the corresponding histograms for Gaussian and Brownian noise there is no directional bias. This bias for natural images is also observed for gradient orientation by among others [42] but is perhaps slightly more pronounced in the 2nd order case. It is not an unexpected effect as most collections of natural images are acquired with the x-axis more or less horizon-aligned. It is, however, a clear effect of the fact that most structures (man-made or not) in images of this type adhere to the same horizon bias, i.e. have an abundance of structures with dominant horizontal or vertical orientation. It should be noted that the invariant shape index is unaffected by this bias.
- The logged histogram of curvedness (Fig. 3, bottom row, right) is a close to a straight line suggesting the distribution itself to be near exponential.
- As demonstrated in several independent studies [9,49,46,17] the statistics of natural images are non-Gaussian. That this is also the case for the three statistics presented above is easily verified through Fig. 3.

2.3. Shape index maximum likelihood metameres

In the previous sections, we have discussed the shape index, curvedness, principal direction as an alternative parameterisation of local 2nd order structure in images and given novel statistics of the three parameters for specifically natural images. In this section, we further investigate the structure of natural image 2nd order structure through the shape index as the factored jet-space of intrinsic structure. In this, we will deliberately ignore curvedness and principal direction as they essentially only convey variations of the 'fundamental' structure given by the shape index.

The basis of our investigation is the fact that although different image patches may measure to derivatives yielding the same shape index there is no guarantee that the patches are otherwise identical. These differences can be seen across points within single images, across images, and images types (noise, natural, medical etc). The five illustrations above the shape index interval in Fig. 1 are such examples of structures with specific shape indices but are in no way unique. Our aim is to investigate the notion of typical or canonical image structures for natural images – to underline the uniqueness of the results control experiments are presented for Gaussian and Brownian noise.

Borrowing from colour science, Koenderink [26,31] formalised this identity under measurements through the concept of *metamerism* [27]. Although the *measured* jet is a good characterisation of the local structure in an image, it does not fully determine the measured image. Summarising, several image patches can and will measure to the same jet or point in jet-space. These patches constitute an equivalence or *metamery* class under the applied filters. A proper characterisation of the 'true' structure represented by a jet should consider this entire class of image patches and not just individual fiducial members. This is, however, a daunting task

and Koenderink has suggested [26,31], that the best way to investigate the nature of the structure represented by a metamery classes is through a simple iconic or canonical representative of the class. Koenderink further suggested (more or less) that these icons should be selected as the element in a metamery class with the smallest range of intensity values. We have earlier studied range minimisation and several other candidate rules for icon selection all based on minimisation of some measure of complexity – complexity was defined in terms of a norm – either based on image luminance or image 'roughness'. A full description can be found in [17] where some of the main conclusions are: (i) while the luminance range minimisers for low order jets are quite representative of natural image structure, for higher order they are distinctly less so, (ii) roughness minimisers produce quite natural looking icons with the well-known Total Variation minimiser [50] as the most successful. In summary, icons can be produced using complexity minimisers but there are, however, two main problems with this approach: (i) the choice of complexity minimiser can and will affect the qualitative nature of the icons, and (ii) a complexity measure impose an underlying model distribution [37] of natural images that at worst is plain wrong and at best only models some aspects of the actual distribution of natural images.

To avoid these problems and as a refinement of Koenderink's original proposal, we proposed Geometric Texton Theory (GTT, [19]) where icons are selected as the maximum likelihood (relative to natural image statistics) elements of metamery classes – that is the most likely or the modal patch in high-dimensional patch space. This approach avoids unnecessary or simplified assumptions about the underlying distribution of natural images and instead uses a large database of images to model it indirectly.

In this section, we will present the 'raw' ML metameres and discuss them as such – in Section 3.2, we discuss their potential to induce a categorisation of the shape index interval.

The methodology used to calculate the ML icons is similar to that described in [17,36]. Summarising, an icon is calculated for each of 31 equally sized and spaced bins across the shape index. Results are calculated independently for Gaussian noise, Brownian noise, and natural images.

The results for the three different images types can be found in Fig. 4 (Gaussian noise), Fig. 5 (Brownian noise), and Fig. 6 (natural images). In all figures, the maximum likelihood metameres follow the binned shape index from top to bottom, left to right – the top left ML metamere corresponds to a shape index of approximately $-\frac{\pi}{2}$, the central to 0, and the bottom right to $\frac{\pi}{2}$. Individual patches are displayed as 10-level contour plots. Please note that due the principal direction-dependent patch extraction (see [36]), patches appear as if rotated ninety degrees as one passes through the central saddle-like bin.

Initially, we note that the Gaussian and the Brownian icons, except for noise, match the analytical predictions [19] based on corresponding bin centres. This confirms that the overall ML framework is working as intended and reinforce the validity of the natural image ML estimates. It should, however, be noted that the distribution of natural image patches is more complex than that of the Gaussian distributions from the control experiments. In accordance with expectations and similar to our earlier studies, the Gaussian and Brownian ML estimates are more noisy than the corresponding natural image estimates.

We further remark that the natural image ML icons are different from both the Gaussian and Brownian control experiments making the result specific to natural images.

Both the Gaussian and Brownian ML icons (although more noisy) come across as slightly more symmetrical across the central bin than the natural image ones. This is also what we found for the shape index histograms (Section 2.2).

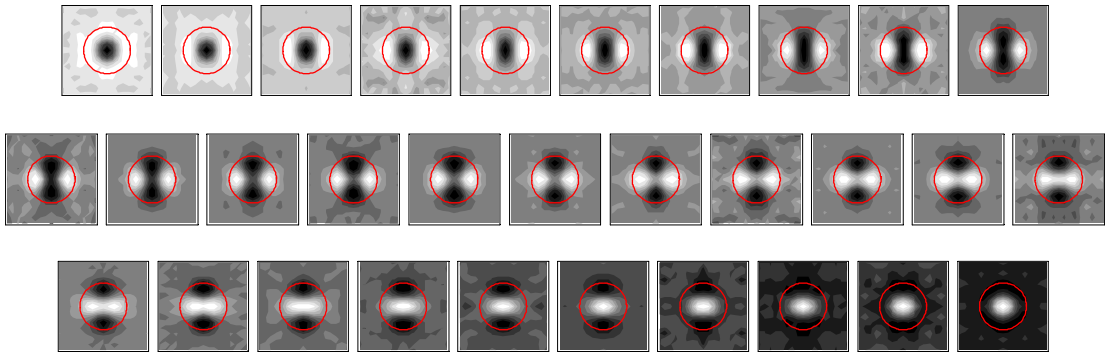

Fig. 4. The ML icons for Gaussian noise. Top left corresponds to shape index $-\pi/2$ and bottom right to $\pi/2$.

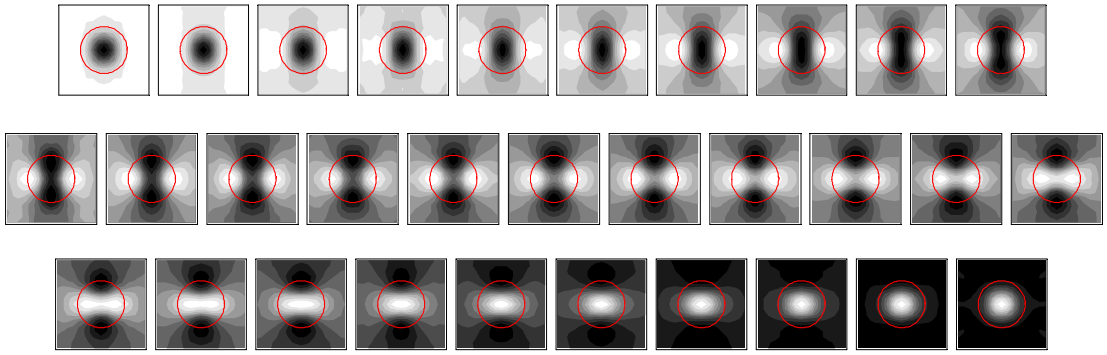

Fig. 5. The ML icons for Brownian noise. Top left corresponds to shape index $-\pi/2$ and bottom right to $\pi/2$.

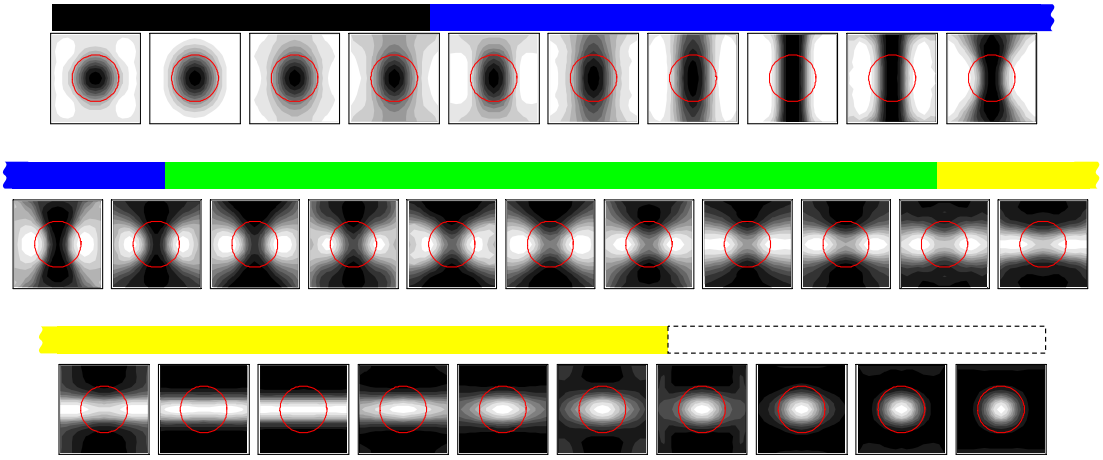

Fig. 6. The ML icons for natural images. Top left corresponds to shape index $-\pi/2$ and bottom right to $\pi/2$. The coloured bars above the icons indicate the geometrically induced categories discussed in Section 3.1.

Compared to both the Gaussian and Brownian results, the natural image icons close to the parabolic part of the shape index are distinctly more line-like. Although all three shape index histograms have concentrations of mass in the vicinity of the parabolic parts the ML icons reveal that only natural images seem be dominated by actual line-like structures. The strong continued lines for parabolic natural image icons could be explained by the fact that natural images normally do not have isolated locally line-like points by more typically long continued line segments.

In terms of distinct qualitative feature types revealed in the natural image icons, we will confine ourselves to naming five: dark blobs, dark bars, saddle-like, light bars, and light blobs. The remaining bins come across as smooth transitions between these primary feature types. Fig. 7 shows where these five central ML icons were extracted from the database of natural images.

The presented results in terms of statistics of the shape index, curvedness, principal directions and the shape index ML icons for natural images are in themselves interesting and can further our understanding when modelling or otherwise working in this domain. They underline reported results [9,46,45] that natural images share features with many 'simpler' images classes and suggested models but still remain distinct and as such not yet fully characterised. In the following, we will use the presented results to pursue a shift from purely quantitative analysis and present ideas and methods to facilitate a transition to a more qualitative understanding of local pure 2nd order structure in natural images.

3. Shape index category systems

The shape index constitutes a natural re-parameterisation of the factored jet-space and we now address the second main topic of this paper – an investigation of category systems (or partitionings of the factored response space) that naturally arise from the geometry and natural image statistics of the shape index descriptor. As described in the introduction, three different avenues will be investigated and the results related.

3.1. Categories from geometry

The simplest avenue to a categorisation of the shape index comes from the 'geometry' of the descriptor itself. Considering the principal curvatures and the definition of the shape index gives rise to five equally spaced landmarks: minimal and maximal umbilic points ($\kappa_1 = \kappa_2$), convex and concave parabolic points ($\kappa_1 \neq 0, \kappa_2 = 0$), and the balanced saddle point ($\kappa_1 = -\kappa_2$). A natural category system based on these five centres/landmarks comes from a simple Voronoi-tessellation [12] of the shape index interval as illustrated in Fig. 8 below. An example of an image coloured according to this category system can be found in Fig. 14 (the illustration will be further commented in the discussion).

Although the category centres of this five category system seem quite natural given an inspection of the shape index, it only fair to consider alternative approaches to forming category systems – the topic of the following two sections. Interestingly enough, these five

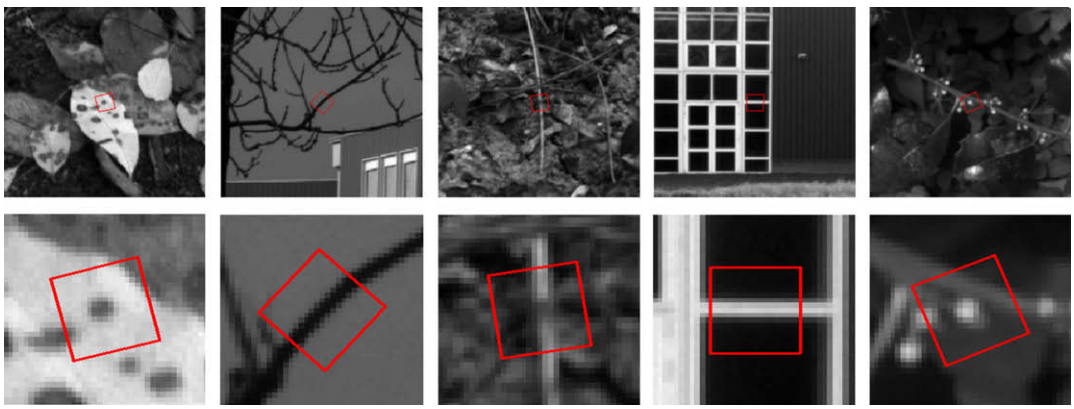

Fig. 7. The context of 5 patches that were chosen as modes – top row is the large scale context and bottom row a zoom on the central part.

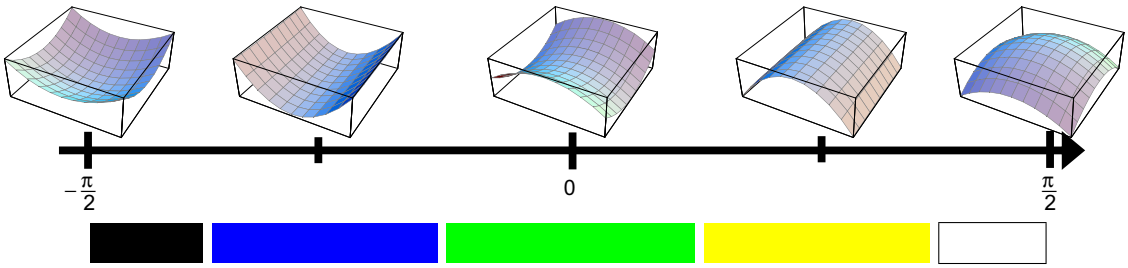

Fig. 8. The shape index real interval with a five category system derived from five natural category centres and simple Voronoi-tessellation. The centres of the categories from left to right are: dark blobs ($\vartheta = -\frac{\pi}{2}$), dark lines ($\vartheta = -\frac{\pi}{4}$), saddles ($\vartheta = 0$), light lines ($\vartheta = \frac{\pi}{4}$), and light blobs ($\vartheta = \frac{\pi}{2}$).

category centres can be reached using another line of argumentation based not directly on the 'geometry' of the shape index but on the symmetries of simple representatives along the shape index interval. Consider as simple representatives along the shape index interval, polynomials that measure to the corresponding shape index. We know that all these representatives have two reflectional symmetries – horizontal and vertical relative to the principal direction. The endpoints of the interval or dark and light umbilics stand out as the only points that are isotropic or have complete rotational symmetry. The parabolic points stand out as the only two points to have a continuous translational symmetry. And finally the saddle point is unique in the sense that is has two diagonal anti-reflectional symmetries – see Fig. 9. From a symmetry point of view, we thus get the same five special points or category centres as above and subsequent Voronoi-tessellation yields the same category system as illustrated in Fig. 8. Symmetry is a strong cue and using symmetry to identify special or simple points is not new [47,55,56,48].

3.2. Categories from geometric texton theory

The maximum likelihood metameres or icons presented in Section 2.3, although interesting in themselves, should be considered as the basis of a category system. Koenderink suggested to use the aforementioned metamerism and (i) to associate with each point of jet space an iconic image from the metamery class of possible images, and (ii) the equivalence relation of 'qualitative identity of icons' gives rise the a partitioning of jet space into features. This icon based partitioning can yield clusters or categories much more versatile that of simple or more direct clustering schemes [17]. The refinement where icons are selected as the maximum likelihood representatives and used to partition response spaced was introduced as Geometric Texton Theory (GTT) and has been applied to several examples of 'simpler' natural image structure [19,15,17]. We will briefly review these results before we proceed to interpret the shape index icons in the context of GTT. An in-depth review of GTT can be found in [17].

Previously published GTT results are summarised in Fig. 10. The topmost left part shows the results for 1D natural image profiles (1D), where the 1-jet is measured yielding two degrees of freedom (DoF). An affine transformation soaks up both DoF and results in a 0-dimensional factored response space with one metamery class. The maximum likelihood metamere or class representative is an approximate step edge. The simplicity of this example thus results in a one-category system.

The topmost right part of Fig. 10 shows three maximum likelihood metameres for the corresponding experiment for natural image patches (2D). Measuring the 1-jet in 2D yields 3 DoF – two of which are soaked up by the affine transformation and one by the fact that all patches are extracted so that their 'x-axis' is parallel to the gradient direction. Again, the result is a 0-dimensional factored response space and the canonical icon is an approximate step-edge. In summary, if one looks at 1st order structure in natural images (profiles or patches), the most likely representative for non-flat points is an approximate step-edge. Qualitatively speaking 1st order structure in natural images is either flat or most probably edge-like.

The bottom part of Fig. 10 gives the results for profiles (1D) where the 2-jet is measured (3 DoF). Again, the affine transformation soaks up two of them – the one remaining DoF is re-parameterised as a phase-like [15] component and binned as described above. In the left part, each row of the tableau corresponds to a maximum likelihood icon for a given phase bin. Thus the horizontal axis is spatial and vertical axis is phase – one profile for each phase bin. The right part of the figure shows the three dominant profiles. The interesting part of this result is that 1D full 2nd order natural image structure fall into one of three qualitative distinct feature types: bar, edge, and pass. In the left tableau the transitions between these occur quite abruptly over a couple of bins which effectively enforces a category structure based on qualitative identity of icons – and thus supports the main idea of GTT.

3.2.1. Results

Reviewing our current results for the shape index of natural images (Fig. 6) in the light of the 1D 2-jet example above, it is, however, clear that we do not get the crisp category structure offered there. Although, the five category centres (dark blob, dark line, saddle, light line, light blob) are clear, the boundaries between

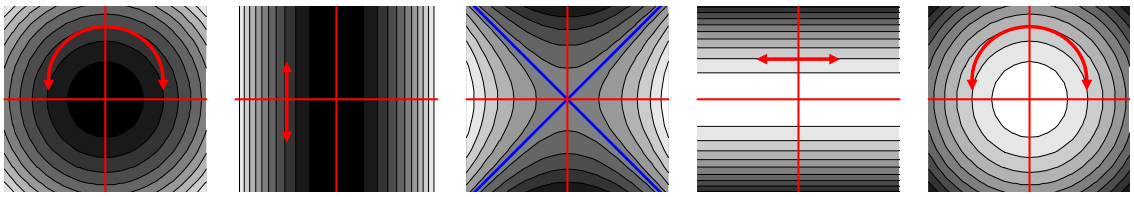

Fig. 9. Contour plots of polynomial representatives for shape indices $\pm\frac{\pi}{2}, \pm\frac{\pi}{4}$, and 0. Red lines represent the lines of the two reflectional symmetries intrinsic to all polynomial representatives along the shape index interval. Curved and normal arrows represent complete rotational and continuous translational symmetries, respectively. The blue line are lines of anti-reflectional symmetry. The symmetries of each of the five shown shape index representatives are unique along the shape index (except of course for their'mould' of opposite sign).

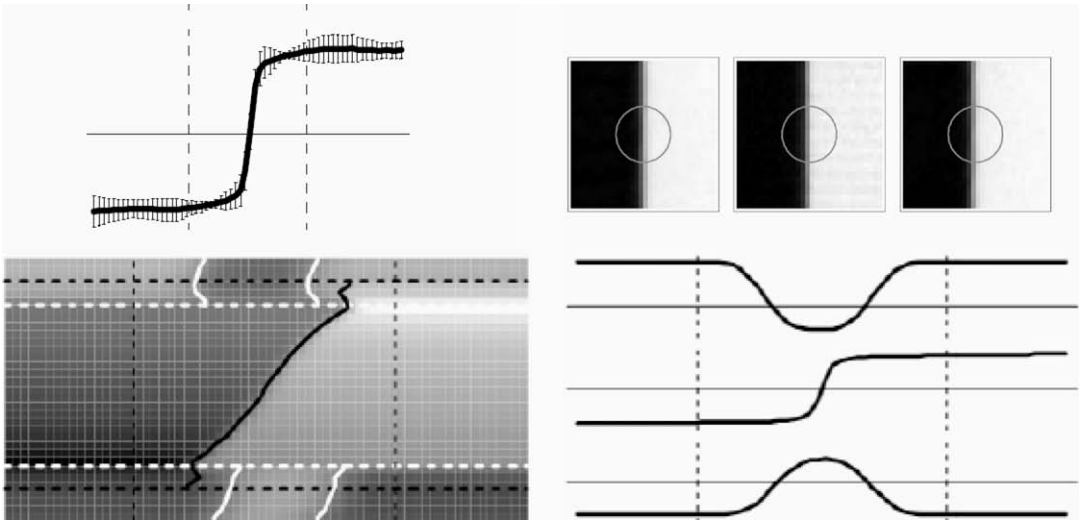

Fig. 10. A summary of previously published GTT results. Top left is the ML icon for 1st order structure in natural image profiles. Top right, 3 repetitions of the corresponding study for natural image patches. Bottom row depict the ML icons for full 2nd order structure in natural image profiles – see main text for details.

them are at best fuzzy – the transitions between category centres are extremely smooth and the full category structure achieved in our 1D study seems elusive. A possible explanation is that the transitions actually are smooth which in turn then questions whether the ML icons can facilitate a well-founded chopping up of jet-space in general.

The ML icons do, however, produce five clearly distinct types of local structure supporting the category system based on the shape index's special points and/or symmetries. In Fig. 6, this category system has been displayed together with the ML icons. If we allow for 1–2 bin wide transition zones (as in the 1D, 2nd order example above), it provides as good a match as any category system based on qualitative equality of icons would.

3.3. Categories from stability with respect to perturbations

Our final approach towards a category structure on the shape index descriptor is based on stability considerations. In a nutshell, a desirable quality of a category system is stability across a wide range of reasonable image perturbations such as noise, change of lighting, viewing angle etc. Stability considerations can either be used to test the stability of already known category systems or as a generator of optimally stable category systems. Below, we will discuss both techniques.

Before we proceed, it is however important to realise that stability with respect to perturbations is perturbation-dependent in the sense that e.g. high noise stability may or may not imply, e.g. view-point stability and vice-versa. Along the same lines of thought the usefulness of such low level stability considerations is also dependent on the high level task that is served by, e.g. feature categories. Results presented below are thus specific to the kinds of perturbations discussed and should not be generalised without care. With that said, we continue to investigate the stability of the geometrically inspired category system derived above and compare it to categories systems that are optimally stable with respect to two types of perturbations: (i) stability under additive Gaussian noise and (ii) cross colour-channel stability for RGB images as described in [13].

Stability with respect to additive Gaussian noise is more or less self-explanatory whereas the cross channel stability deserves a few remarks before proceeding with the details of the experiments. The idea is that the channels of colour images (in this case the R, G, and B channels) are highly correlated although not identical and offers less trivial perturbations than that of simple additive Gaussian noise. Furthermore, we postulate that local features as discussed here to some degree should be consistent across colour channels for (generic) natural images. As noted in [15], the pattern of intensities in different colour channels are quantitatively different but the images are qualitatively very similar.

3.3.1. Methodology

We initially describe the methodology used to investigate category stability with respect to Gaussian additive noise and then review the corresponding colour-channel experiments in this context.

3.3.2. Additive Gaussian noise and overall setup

Given a scalar image I and zero-mean Gaussian noise parameterised by the standard deviation σ, consider an image pair $A = I + N(0,\sigma)$, $B = I + N(0,\sigma)$. Both images are noisy versions of I 'corrupted' by independent realisations of additive Gaussian noise.

Shape index images are calculated for both images. Pairing up co-located pixels, the joint shape index histogram for the two noisy images can be calculated. The two marginals of this histogram of course constitute the shape index histograms for A and B.

The sum of diagonal of the joint shape index histogram are the number of shape index matches between the two corrupted versions of I. Now assume we investigate, e.g. a 5-category system of equal-width bins. Using the joint histogram, the un-normalised stability score is simply the sum of the block-diagonal (the block-diagonal is derived from the original joint histogram matrix using only 5 bins instead of the full 'resolution'). We normalise this score by subtracting the chance of getting identical categories by chance: the inner product of the corresponding block-marginals.

The methodology above described was for one image and one noise level. For the results presented below, all histograms for a given noise level are accumulated across the entire subset of the van Hateren Database discussed in [17,36]. Subsequently, this procedure is repeated for a number of noise levels.

In general, the results will be presented as a function of increasing additive noise. For easier comparison with the cross-channel colour results described below, the actual x-axis of all plots is $1 - \mathit{correlation}$. For each noise level σ, the *correlation* is calculated as the average standard linear correlation coefficient

(Pearson's correlation) between A and B across the entire image database.

In the following, we will investigate the resulting stability scores for a number of different shape index category systems using from two to five categories:

- Equal-width categories. For a given number of categories (2–5), the stability scores of category systems where the categories all have the same width in terms of shape index interval spanned. Directly calculated using the block-diagonal scheme described above.
- Equal-weight categories. For a given number of categories (2–5), the stability score of category systems where all categories have the same amount of 'histogram-mass' in them. Directly calculated using the cumulative histograms and the block-diagonal scheme described above.
- Optimal categories. For a given number of categories (2–5), the category system that has the optimal stability score. For n categories, the complete stability landscape parameterised by $n-1$ category boundaries is calculated and the category system at the global maximum is selected.
- The geometrically inspired category system from Section 3.1. Reference scores for this system are directly calculated using the block-diagonal scheme described above.

3.3.3. Cross-channel colour image experiments

The overall setup is the same as described above for additive Gaussian noise except the perturbed image pairs are given by combinations of the scalar R, G, and B channels. For a given RGB image we have three combinations RG, RB, and GB. Each of these combinations are comparable to a noise level in the Gaussian noise experiment.

As for the Gaussian noise experiments the joint and marginal histograms are accumulated over a database of colour images. Specifically, we use a subset of the McGill Calibrated Colour database gamma corrected as suggested in [43].

For each of the three colour channel combinations, the averaged correlation has been calculated for all images used. The resulting correlations for each of the three channel combinations are: RG = 0.76, RB = 0.66 and GB = 0.77. These scores are fully compatible with the reported camera RGB spectral sensitivities [43] and allow for the colour experiments to be plotted together with the Gaussian results on a $1-correlation$ axis as described above.

3.3.4. Results

The results of both the Gaussian noise and the cross-channel experiments are summarised in Figs. 11–13.

Fig. 11 gives the boundaries of the optimally stable categories as a 'function' of $1-correlation$. Remember that increasing $1-correlation$ effectively express increasing additive noise. The main result is given by the blue curves that indicate the category boundaries that are optimal under perturbation with additive Gaussian. For all noise levels the four boundaries of an optimal 5-category system was calculated. For reference, the dashed red lines indicate the four boundaries of a 5-category equal-width system. The two-coloured dots indicated the optimal category boundaries for each of the three cross-channel colour experiments.

We offer the following immediate comments to the results:

- For low levels of noise or very small perturbations the optimal 5-category system is very close to a equal-width 5-category system. For high levels of noise the optimal 5-category system is actually a 2-category system very similar to a 2-category equal-width system. This effect is due to collapsing category boundaries and fully acceptable.

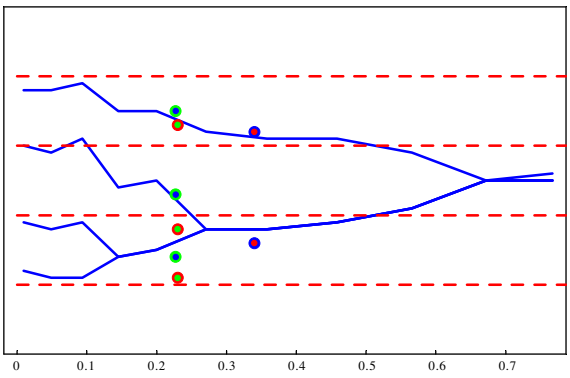

Fig. 11. Optimal category boundaries for shape index categories with respect to additive Gaussian noise. The y-axis spans the shape index and the x-axis is increasing amount of additive noise from left to right (in 'units' of $1-correlation$). The blue curves indicate the position of the category boundaries that yield optimal stability to the added noise as a'function' of amount of added noise. The dashed red lines indicate the four category boundaries of an equal-width 5-category reference system. The red/blue, red/green, and blue/green dots indicate the category boundaries for each of the three combinations of colour-channels. See further details in the main text.

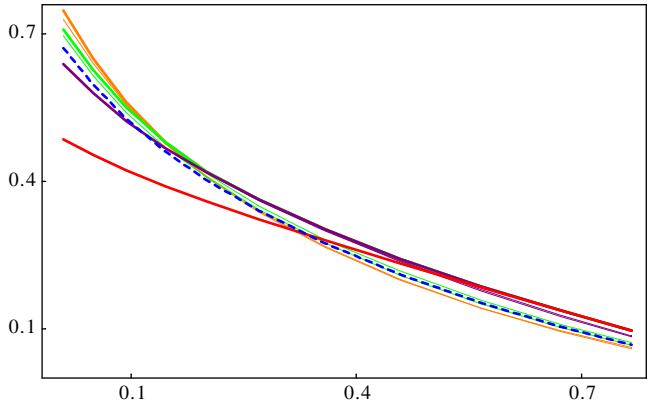

Fig. 12. Stability scores for a suite of category systems. The y-axis is normalised stability score – higher is better. The x-axis is again $1-correlation$ and indicative of the amount of additive noise. The red curve indicates the performance of an optimal 2-category system as a function of additive noise. The purple represents an optimal 3-category system, the green 4 optimal categories, and brown 5 optimal categories. The dashed blue indicate the performance of the geometrically based 5-category system derived in Section 3.1. Finally, the thin (and hard to see) red, purple, green, and brown curves represent the performance of uniform size and weight 2-, 3-, 4-, and 5-category systems. See further details in the main text.

- Elaborating on the above comment across all levels of noise, the results essentially show that as noise is added, the system is collapsing five categories into two. Along the way 'bifurcations' happen at approximately equal-width n-category systems.
- The cross-channel colour experiments follow the corresponding (same correlation) noise experiments fairly closely. The optimal number of categories is an exact match to that of the Gaussian noise experiments. The position of the category boundaries match the corresponding Gaussian noise ones fairly well for two of the channel combinations – the third one is slightly of.

Fig. 12 gives the stability scores of a variety of category systems as a function of $1-correlation$ and we offer the following immediate comments to the results (ignoring the thick dashed blue curve for now):

- The stability scores of the optimal 2-, 3-, 4-, and 5-category systems converge as noise increases. This makes perfect sense – as we have seen in Fig. 11 the optimal systems all collapse into the optimal 2-category system as noise increases and thus eventually have identical stability scores.

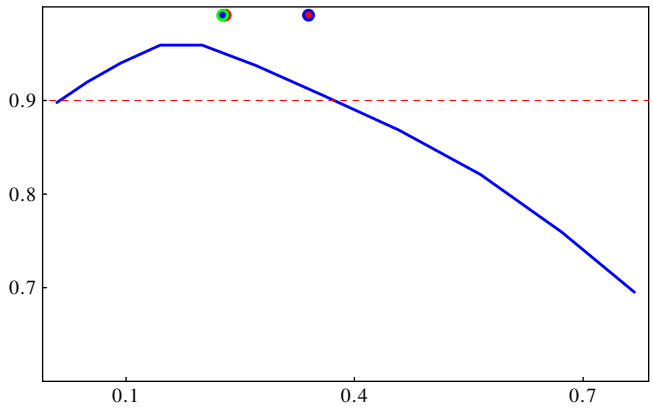

Fig. 13. The relative performance of the optimal 5-category system and the geometrically inspired 5-category system discussed in Section 3.1. The *y*-axis is the ratio of the geometrical system over the optimal system stability scores. Again, the *x*-axis is 1 − *correlation* and indicative of the amount of additive noise. The dashed red line indicate a relative performance of 90%. The coloured dots indicate the *x*-position of the cross-colour-channel experiments – their *y*-coordinates are fiducially fixed to 1. See further details in the main text.

- For low levels of noise the graphs suggest that more categories yield better stability score. We have verified this trend for larger numbers of categories. Essentially, it is down to the properties of the stability score itself. This score is best understood as a measure of how much information we are successfully communicating about a signal through a noisy channel [51]. For a mildly distorting channel, it is optimal to communicate as detailed information as possible. As noise in the channel increases, it is optimal to communicate roughly quantised information.
- The equal-width and equal-weight scores are roughly identical to the optimal one for low noise levels. As noise increases the optimal category systems all collapse into 2-category ones and tend to outperform their corresponding equal-width and -weight one that of course do not collapse.

The thick dashed blue curve in Fig. 12 indicates the stability score of the 5-category geometrically inspired category system described in Section 3.1. This category system is, not surprisingly, less stable than the optimal 5-category system. Fig. 13 shows the performance of the geometrical 5-category system relative to the optimal 5-category system. It indicates that from low noise levels to a noise level corresponding to $(1 - \mathit{correlation}) \approx 0.4$ the geometrical category system is within 10% of the performance of optimal system although it remains a 5-category system throughout. Furthermore, all the cross-channel colour experiments fall within this 10% performance band as indicated by the coloured dots in Fig. 13.

4. Discussion

The novel contributions of this paper are:

- Statistics for the shape index, curvedness, and principal direction for a large database of natural images yielding results clearly distinct from that of Gaussian random noise controls. Furthermore, we have re-argued Koenderink's point that the shape index is a natural, invariant, and decoupled re-parameterisation of 2nd order (image) fundamental structure. In combination with the curvedness and principal direction, we have a very intuitive triple describing essential intrinsic and extrinsic 2nd order structure.
- Further insight into the shape index for natural images specifically was obtained through maximum likelihood metameres as a function of the shape index. Again, these results were unique to natural images and clearly distinct from that of Gaussian and Brownian control experiments.
- Three studies of a potential category system on the shape index:
  - One based on Voronoi cells around landmark values of the shape index.
  - One based on qualitative similarity of ML icons using Geometric Texton Theory. Although no crisp category came from this study it reasserted five unique category centres and supported the category system from the first study.
  - One based on the idea that stability is a desirable quality of a category system. For reasonable amounts of perturbations equal-width category systems came out as optimal. For higher noise levels and the cross-channel colour experiments, the optimal category systems collapsed into fewer categories.

Given the results summarised above, we put forward the geometrically inspired 5-category system (Fig. 8) as a good candidate for future studies and applications. It yields an alphabet of five 2nd order feature types: dark blobs, dark lines, saddles, light line, and light blobs. The system is a reasonable match to the ML icons and performs within 10% of an optimal category system based on stability considerations across a range of signal-to-noise levels while still maintaining the full five categories. The category centres are intuitive and easy to pick out – either in terms of intrinsic geometry or symmetries.

Fig. 14 gives a simple example of a dense labelling/colouring of the pixels in an image according to the suggested category system. In the rightmost image, points that are near-flat in the 2nd order

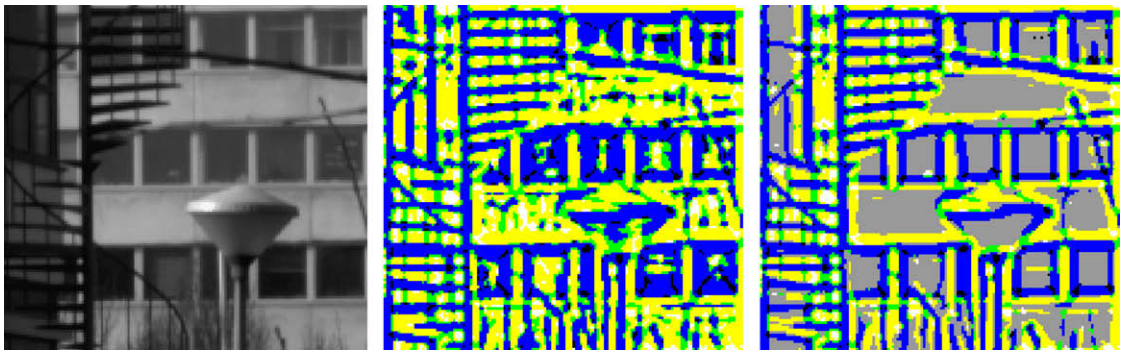

Fig. 14. An image from the van Hateren database. The middle image illustrates how each point would be categorised using the geometrically inspired category system from Section 3.1. The categories are dark blob (black), dark line (blue), saddles (green), light lines (yellow), and light blob (white). The right image is identical to the middle one except near-flat points are coloured grey – flatness in the second order sense is realised through a manually selected threshold on the curvedness.

sense have been coloured grey. As this example suggests the resulting labelling offers an interesting insight into the salient structures of the image. This may well serve as good supplement for descriptions of local structure such as the SIFT encoding [39] that currently relies solely on an alphabet of quantised gradient orientation. One could imagine a more powerful local descriptor using a SIFT-like framework but based on a 2nd order alphabet like the one presented here.

We have previously studied the full 2-jet and offered the 2nd order local-image-structure solid [16] as a factored response space comparable to that of the shape index for the pure 2nd order. Preliminary studies of potential category structures for that can be found in [14,18] and naturally support and generalise the category system put forward above.

Acknowledgement

EPSRC-funded project 'Basic Image Features' EP/D030978/1.

References

[1] J. Aghajanian, Patch-based face recognition using latent identity variables, in: The Inaugural BMVA Students Paper Meeting, 2007.
[2] A.J. Bell, T.J. Sejnowski, The "independent components" of natural scenes are edge filters, Vision Research 37 (23) (1997) 3327–3338.
[3] J. Canny, A computational approach to edge detection, IEEE Transactions on Pattern Analysis and Machine Intelligence 8 (6) (1986) 679–698.
[4] V. Caselles, R. Kimmel, G. Sapiro, Geodesic active contours, in: ICCV95, 1995, pp. 694–699.
[5] F. Casorati, Nuova definitione della curvatura delle superficie e suo confronto con quella di gauss, Rend. Maem. Accd. Lomb. 1867/1868.
[6] J.G. Daugman, Uncertainty relations for resolution in space, spatial frequency, and orientation optimized by two-dimensional visual cortical filters, Journal of the Optical Society of America A (1985) 1160–1169.
[7] M. de Bruijne, M. Nielsen, Shape particle filtering for image segmentation, in: C. Barillot, D.R. Haynor, P. Hellier (Eds.), Medical Image Computing & Computer-Assisted Intervention, Lecture Notes in Computer Science, Vol. 3216, springer, 2004, pp. I:186–175.
[8] A.A. Efros, W.T. Freeman, Image quilting for texture synthesis and transfer, in: Proceedings of the 28th Annual Conference on Computer Graphics and Interactive Techniques, 2001, pp. 341–346.
[9] D.J. Field, Relations between the statistics of natural images and the response properties of cortical cells, Journal of the Optical Society of America 4 (12) (1987) 2379–2394. Dec..
[10] L.M.J. Florack, B.M. ter Haar Romeny, J.J. Koenderink, M.A. Viergever, Cartesian differential invariants in scale-space, Journal of Mathematical Imaging and Vision 3 (4) (1993) 327–348. November.
[11] J. Folkesson, E. Dam, P. Pettersen, O.F. Olsen, M. Nielsen, C. Christiansen, Locating articular cartilage in MR images, Proceedings of SPIE 5747 (2005) 1484.
[12] P. Gärdenfors, Conceptual Spaces: The Geometry of Thought, MIT Press, 2000.
[13] L.D. Griffin, Deduction of feature categories from colour images, in: Spatial Vision, vol. 18(4), Brill Academic Publishers, 2005.
[14] L.D. Griffin, An analogy between colour vision and local spatial vision: filters, factors and categories, Cognitive Processing, submitted for publication.
[15] L.D. Griffin, M. Lillholm, Image features and the 1-d, 2nd order gaussian derivative jet, Proceedings of Scale Space 2005 (2005) 26–37.
[16] L.D. Griffin, The 2nd order local-image-structure solid, IEEE Transactions on Pattern Analysis and Machine Intelligence 29 (8) (2007) 1355–1366.
[17] L.D. Griffin, M. Lillholm, Hypotheses for image features, icons and textons, International Journal of Computer Vision 70 (3) (2006) 213–230.
[18] L.D. Griffin, M. Lillholm, Feature category systems for 2nd order local image structure induced by natural image statistics and otherwise, Proceedings of SPIE (2007).
[19] L.D. Griffin, M. Lillholm, M. Nielsen, Natural image profiles are most likely to be step edges, Vision Research 44 (4) (2004) 407–421. February.
[20] C. Harris, M.J. Stephens, A combined corner and edge detector, in: Alvey88, 1988, pp. 147–152.
[21] J. Huang, D. Mumford, Statistics of natural images and models, in: CVPR99, 1999, pp. I:541–I:547.
[22] D.H. Hubel, T.N. Wiesel, Receptive fields and functional architecture of monkey striate cortex, Journal of Physiology 195 (1968) 215–243.
[23] A. Hyvärinen, P.O. Hoyer, A two-layer sparse coding model learns simple and complex cell receptive fields and topography from natural images, Vision Research 41 (18) (2001) 2413–2423.
[24] J.P. Jones, L.A. Palmer, The two-dimensional spatial structure of simple receptive fields in cat striate cortex, Journal of Neurophysiology 58 (6) (1987) 1233–1258.
[25] J.J. Koenderink, The structure of images, Biological Cybernetics 50 (1984) 363–370.
[26] J.J. Koenderink, What is a feature?, Journal of Intelligent Systems 3 (1) (1993) 49–82
[27] J.J. Koenderink, The structure of colorimetry, in: G. Sommer ,Y.Y. Zeevi (Eds.), Alebraic Frames for Perception–Action Cycle, number 1888 in LNCS, Springer-Verlag, 2000, pp. 69–77.
[28] J.J. Koenderink, A.J. van Doorn, Receptive-field families, Biological Cybernetics 63 (4) (1990) 291–297.
[29] J.J. Koenderink, A.J. van Doorn, Generic neighborhood operators, IEEE Transactions on Pattern Analysis and Machine Intelligence 14 (6) (1992) 597–605.
[30] J.J. Koenderink, A.J. van Doorn, Receptive field assembly specificity, Journal of Visual Communication and Image Representation 3 (1) (1992) 1–12.
[31] J.J. Koenderink, A.J. van Doorn, Metamerism in complete sets of image operators, in: Advances in Image Understanding'96, 1996, pp. 113–129.
[32] J.J. Koenderink, A.J. van Doorn, Image processing done right, in: A. Heyden, G. Sparr, M. Nielsen, P. Johansen (Eds.), ECCV 2002, LNCS, vol. 2350, Springer, Copenhagen, 2002, pp. 158–172.
[33] J.J. Koenderink, A.J. van Doorn, Surface shape and curvature scales, Image and Vision Computing 10 (8) (1992) 557–565.
[34] J.J. Koenderink, A.J. van Doorn, Local structure of Gaussian texture, IEICE Transactions on Information and Systems 86 (7) (2003) 1165–1171.
[35] T. Leung, J. Malik, Representing and recognizing the visual appearance of materials using three-dimensional textons, International Journal of Computer Vision 43 (1) (2001) 29–44.
[36] M. Lillholm, L.D. Griffin, Maximum likelihood metameres for local 2nd order structure of natural images, in: Scale Space and Variational Methods in Computer Vision, LNSC, Vol. 4485, Springer, 2008, pp. 394–405.
[37] M. Lillholm, M. Nielsen, L.D. Griffin, Feature-based image analysis, International Journal of Computer Vision 52 (2/3) (2003) 73–95.
[38] T. Lindeberg, Feature detection with automatic scale selection, International Journal of Computer Vision 30 (2) (1998) 79–116.
[39] D.G. Lowe, Distinctive image features from scale-invariant keypoints, International Journal of Computer Vision 60 (2) (2004) 91–110. November.
[40] S. Mallat, A theory for multiresolution signal decomposition: the wavelet representation, IEEE Transaction on Pattern Analysis and Machine Intelligence 11 (7) (1989) 674–693. July.
[41] D. Marr, E. Hildreth, Theory of edge detection, Proceedings of the Royal Society of London. Series B, Biological Sciences 207 (1167) (1980) 187–217.
[42] A.J. Nasrallah, L.D. Griffin, Gradient direction dependencies in natural images, Spatial Vision 20 (3) (2007) 277–299.
[43] A. Olmos, F.A.A. Kingdom. Mcgill calibrated colour image database. Available from: <http://tabby.vision.mcgill.ca/>.
[44] B.A. Olshausen, D.J. Field, Natural image statistics and efficient coding, Network-Computation in Neural Systems 7 (2) (1996) 333–339.
[45] K.S. Pedersen, M. Lillholm, Brownian images: A generic background model, in: Proceedings of ECCV'04 Workshop on Statistical Learning in Computer Vision, 2004.
[46] K.S. Pedersen, Statistics of Natural Image Geometry, Ph.D., University of Copenhagen, 2003.
[47] D. Reisfeld, Y. Yeshurun, Robust detection of facial features by generalized symmetry, Pattern Recognition, vol. 1. Conference A: Computer Vision and Applications, Proceedings., 11th IAPR International Conference on, 1992, pp. 117–120.
[48] G. Rhodes, M. Peters, K. Lee, M.C. Morrone, D. Burr, Higher-level mechanisms detect facial symmetry, Proceedings: Biological Sciences 272 (1570) (2005) 1379–1384.
[49] D.L. Ruderman, W. Bialek, Statistics of natural images: scaling in the woods, Physical Review Letters 73 (6) (1994) 100–105. August.
[50] L.I. Rudin, S. Osher, E. Fatemi, Nonlinear total variation based noise removal algorithms, Physica D (1992) 259–268.
[51] K. Sayood, Introduction to Data Compression, Morgan Kaufman, 2000.
[52] F. Schaffalitzky, A. Zisserman, Viewpoint invariant texture matching and wide baseline stereo, Proceedings of ICCV 2 (2001) 636–643.
[53] J.H. van Hateren, A. van der Schaaf, Independent components filters of natural images compared with simple cells in primary visual cortex, Proceedings of the Royal Society, London Series B 265 (1998) 359–366.
[54] M. Varma, A. Zisserman, A statistical approach to texture classification from single images, International Journal of Computer Vision 62 (1) (2005) 61–81.
[55] J. Wagemans, Detection of visual symmetries, Spatial Vision 9 (1) (1995) 9–32.
[56] J. Wagemans, Characteristics and models of human symmetry detection, Trends in Cognitive Sciences 1 (9) (1997) 346–352.
[57] A.P. Witkin, Scale space filtering, in: Proceedings of the Eighth International Joint Conference on Artificial Intelligence, vol. 2, Karlsruhe, Germany, 1983, pp. 1019–1023.
[58] L. Wolf, X. Huang, I. Martin, D. Metaxas, Patch-based texture edges and segmentation, Lecture Notes in Computer Science 3952 (2006) 481.
[59] R.A. Young, The Gaussian derivative theory of spatial vision: analysis of cortical receptive field line-weighting profiles, Gen. Motors Res. Tech. Rep, GMR-4920, 1985.
[60] S.C. Zhu, C. Guo, Y. Wang, Z. Xu, What are textons?, International Journal of Computer Vision 62 (1) (2005) 121–143
[61] S.C. Zhu, Y. Wu, D. Mumford, Minimax entropy principles and its application to texture modeling, NeurComp 9 (8) (1997) 1627–1660.